Research paper

Regression behavior of polylactic acid manufactured by fused filament fabrication for hybrid rocket propulsion

Kohei Ozawa*†, Han-wei Wang*, Takefumi Inenaga*, and Nobuyuki Tsuboi*

*Kyushu Institute of Technology, 1-1, Sensui-cho, Tobata-ku, Fukuoka, 803-0818 JAPAN
Phone: +81-93-884-3418
†Corresponding author: ozawa.kohei582@mail.kyutech.jp

Received: April 14, 2021, Accepted: July 16, 2021

Abstract

Advanced closed-loop control of thrust and mixture ratio of hybrid rockets is planned by combing a fuel mass flow rate control technique with a real-time fuel regression measurement. The latter technique is enabled by a multi-material-additive-manufactured solid fuel with an integrated sensor probe structure. This work investigated the fuel regression behavior of polylactic acid (PLA) fuel used for the main material of this type of solid fuels. Rectangular slab fuels and cylindrical fuel grains were manufactured by Fused Filament Fabrication (FFF) and fired in an optically accessible slab burner and a lab-scale motor, respectively. The cylindrical fuel grains had more than 2 times larger regression rates than rectangular slab fuels even with the same PLA filament. One of the main factors causing this large difference can be an anisotropy in the fuel regression rate behavior of the solid fuels manufactured by FFF.

Keywords: hybrid rockets, additive manufacturing, fused filament fabrication, regression rate, anisotropy

1. Introduction

One of the challenges in conventional hybrid rocket propulsion is the large dependency of fuel regression on oxidizer flow causing a residual propellant and a drop in specific impulse[1),2)]. This characteristic leads to a possibility of causing a large decrease in Delta-V compared to liquid or solid propulsion. The residual propellant problem can be classified into systematic and random errors[2)] from the median fuel regression behavior due to the uncertainty in the quality control of rocket motors and the randomness given by combustion and turbulent phenomena in thermo-fluid dynamics, respectively. The former type of errors requires more severe quality control which increases the production and operation costs, but the other type of errors remains even after the strict quality control.

To solve this residual problem, the authors propose the closed-loop control of hybrid rocket propulsion. Thrust control and remaining propellant management are realized by control and measurement of fuel regression in addition to those of the oxidizer flow. Fuel regression rate is modulated by controlling oxidizer mass flow rates from two injectors giving different fuel regression behaviors. A few types of regression rate control methods were proposed[3)], and especially for altering-intensity swirling oxidizer flow type (A-SOFT), the modulation of regression rate was demonstrated by using the independent control of axial and swirling oxidizer injection[4)].

A few methods for time-resolved fuel regression or fuel mass flow rate measurement were also proposed and demonstrated[5)-9)]. In these options, the miniature resistive regression and ablation sensor (MIRRAS)[6)], which is a representative sensor of resistor-based methods, and ultrasound sensors have potential applicability for the real-time measurement on a launch vehicle or spacecraft. However, these methods also have common difficulties to access the regressing surface for complex solid fuel surface, such as a regression surface of swirling hybrids with a small spiral pitch[10)] and complex fuel grains of the cascaded multistage impinging-jet (CAMUI) type[11)] or end-burning types[12)].

One of the solutions to improve this drawback of MIRRAS is to integrate the sensor probe structure into the solid fuel. This integration is possible by a multi-material 3D printer, an electrically insulating polymer for the main material of the solid fuel, and an electrically conductive

polymer composite for a resistor circuit in the fuel. The proposed fuel regression measurement system detects fuel regression also with a rung breakage of the ladder-shaped resistor at the fuel regression surface as for MIRRAS probes. The authors refer to solid fuels into which a function is integrated as "functional solid fuels". The function of fuel regression measurement has already been demonstrated with a ladder-shaped resistor structure manufactured by a multi-material Fused Filament Fabrication (FFF) 3D printer, an electrically insulated polylactic acid (PLA) filament, and a conductive PLA-based composite filament[13),14)]. The advantage of this integration is in the weight reduction of the measurement system, small pitch local regression measurement without human error factors, and the wide range of applicability including complex shapes of solid fuel of fuel surface owing to the flexibility of the sensing circuit wiring inside the fuel.

Before demonstrating the advanced closed-loop control of hybrid rocket propulsion using the proposed PLA-based solid fuel, from the aspects of the engine design and the safety in experiment operations, it is necessary to characterize the dependency of its fuel regression on oxidizer mass flux, which has not been found in previous investigations. The purposes of this work are to acquire the space-time averaged fuel regression behavior for axial oxidizer injection and find its characteristics unique to solid fuels manufactured by FFF.

2. Firing experiments

2.1 Oxidizer feed system

Figure 1 depicts a piping and instrumentation diagram of the oxidizer feed system used in the experimental campaign. There are three feed lines for the purge nitrogen, gaseous oxygen (GOX) for ignition, and the main oxidizer supply. All the pressure gauges and thermocouples are PGS-100KA models by Kyowa Electric Instruments Co., Ltd. and K-type thermocouples, respectively. A Coriolis mass flow meter QO1 measures the instantaneous mass flow rate of the gas supplied. Gaseous mass flow rate is also measured by the set of a choked orifice, two pressure gauges PG2, PG3, and a thermocouple T2 in two runs using cylindrical grains. This choke orifice was calibrated by steady-state data of QO1 during flow tests. It should be noted that the Coriolis mass flow meter has a transient response delay of approximately 0.64 s and 0.91−1.33 s to reach a steady-state on the rise and the fall compared to the measurement based on the choked orifice. The amplified analog data are converted into digital data with the USB-6343. An in-house LabVIEW software records data at a sampling rate of 1 kHz.

2.2 Slab burner

Figure 2 depicts the cross-sections of the slab burner used

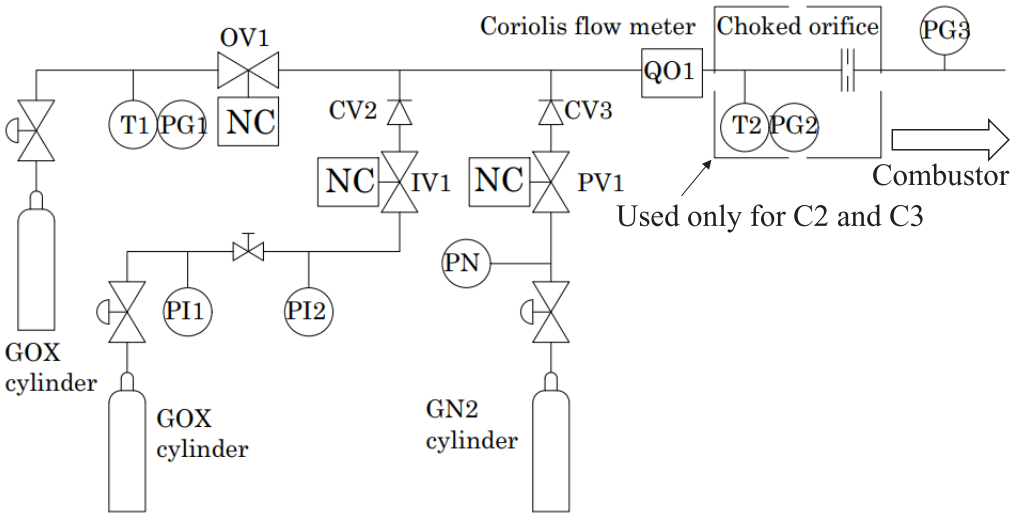

Figure 1 Piping and instrument diagram of the oxidizer feed system.

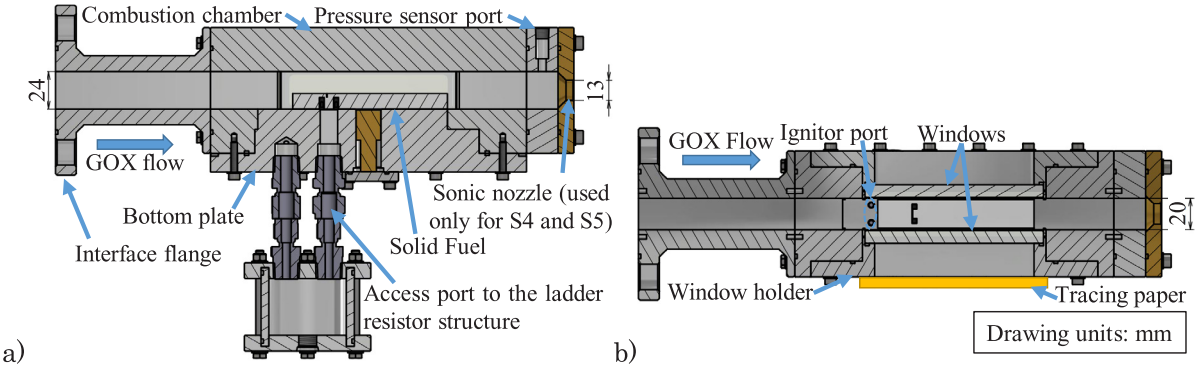

Figure 2 Cross-sections of the slab burner: a) side view; b) top view.

for the firing experiments of the slab fuels. This slab burner has glass windows on both sides. A backlight and tracing paper are placed at one side for the backlighting of scattered light while the fuel regression inside the channel is observed by a video camera from the other side. The slab burner has a 20×24 mm straight rectangular channel without large steps. This slab burner has an option to mount a pressure gauge and a brass nozzle to increase the chamber pressure. The slab fuel is fixed on the bottom plate with instant glue. This plate contains a slit to allow access by a pressure vessel mounted below to the circuit structure interface of the solid fuel. A hermetically sealed wire connector at the pressure vessel ensures airtightness of the burner and electric access inside the burner. There are two ports for ignition wires; however, the ignition wires are routed through the nozzle exit, except for in the first run of experiments. In the upstream of the slab burner, a straightener was installed to eliminate the swirling motions of the flow into the burner.

2.3 Test motor

Figure 3 depicts the drawings of the test motor for the cylindrical fuel grains. This test motor does not have a metal chamber so that the cylindrical grain maintains airtightness and has the role of the combustion chamber by itself. This design to expose the side face of the grain is intended to make it easier to access the interface of ladder-shaped resistors, but time-resolved regression measurement was not carried out in this series of firing experiments. The test motor has a stainless post-chamber plate with a pressure gauge port to measure chamber pressure and a brass nozzle plate with a sonic nozzle of 8 mm diameter. The fuel grain has 13.4 mm, 53.4 mm, and 100 mm inner and outer diameters and lengths, respectively.

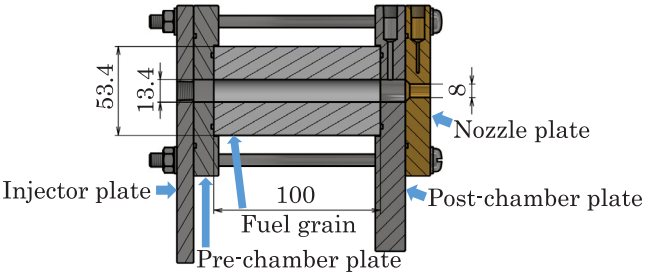

Figure 3 Cross-section of the cylindrical test motor (drawn in mm).

2.4 Optical measurement system

During the firing experiments of the slab burner, high-speed videos of fuel regression are acquired to evaluate the time-history of fuel regression in the post-experimental analysis. Figure 4 illustrates a schematic of the optical system setup. The channel of the slab burner is illuminated by a strong backlight from a modified metal halide lamp (UF3250NAC by Ushio Lighting, Inc.). The backlight from this lamp moderates the brightness of the diffusion flame in the channel and allows the post-experimental analysis program to easily identify the height of the solid fuel surface. The backlight is scattered through a piece of tracing paper placed on the window. Sticker-type rulers are placed on the glass window facing the video camera.

Two types of high-speed cameras are used in the experiments of the slab burner. The first is the FX6000 by NAC Image Technology (Camera 1). This camera is capable of recording color video at 10,000 fps with a resolution of 512×248 pixels (or at 20,000 fps with a resolution of 512×120 pixels) for approximately 5.3 s. The second is the OS8-V3-S3 by IDT (Camera 2). This model is capable of recording monochrome videos for approximately 8.55 s at 7,000 fps with a resolution of 1,600×320 pixels. An AI AF Nikkor 50 mm f/1.8D lens with a minimum f-number of 1.8 is mounted on both cameras. The high-speed camera is triggered in the experimental sequence.

2.5 Solid fuels

Figure 5 presents the three designs of the prototype slab fuels with ladder-shaped resistors normal to the top surface of the slab. The slab fuels tested are 98 mm in length, 18 mm in width, and 5.55–10.20 mm thick. The material for the ladder-shaped resistor structure is CDP11705 by Protoplant, Inc. Its time-resolved fuel regression measurement function was demonstrated[13),14)], but the results of the resistor-based measurement are not used in this work. A Raise3D Premium PLA filament is used for

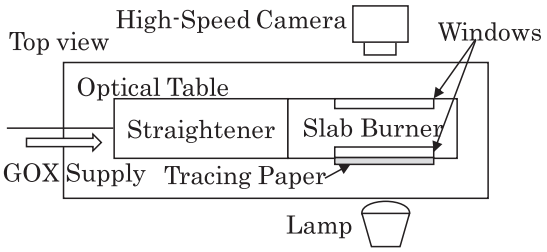

Figure 4 Schematic of the optical setup.

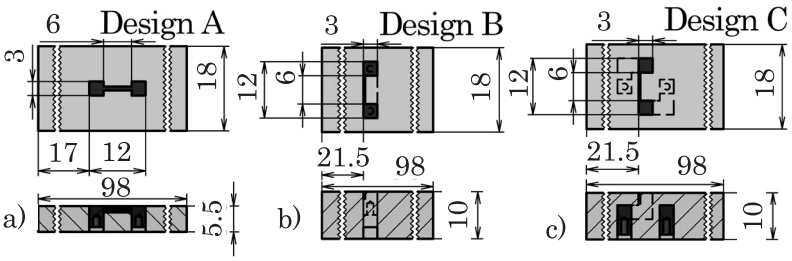

Figure 5 Schematics of slab fuels (drawn in mm): a) Design A; b) Design B; c) Design C.

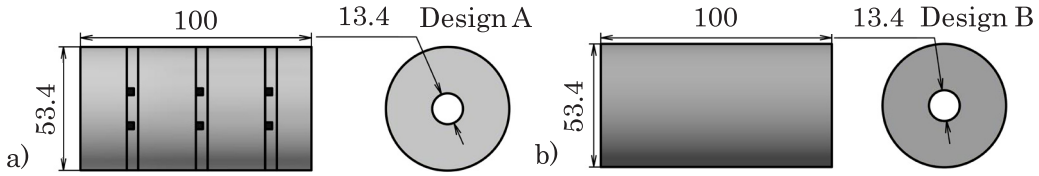

Figure 6 Schematics of cylindrical fuels (drawn in mm): a) Design A; b) Design B.

Table 1 Experimental conditions.

Engine type	Run #	Fuel design	Camera #	OV1 open/close [s]	PV1 open [s]	Ignitor on/off [s]	Camera trigger [s]
Slab burner	S1	A	2	0.0/+5.0	+5.2	−3.0/−1.5	−3.0
	S2	B	1	0.0/+5.0	+5.2	−3.0/−1.5	0.0
	S3	C	1	0.0/+5.0	+5.2	−3.0/−1.5	0.0
	S4	C	1	0.0/+5.0	+5.2	−3.0/−1.5	0.0
	S5	C	2	0.0/+5.0	+5.2	−3.0/−1.5	−3.0
Cylindrical grain	C1	A	N/A	0.0/+5.0	+5.2	−3.0/−1.5	N/A
	C2	B	N/A	0.0/+5.0	+6.0	−3.0/−1.5	N/A
	C3	B	N/A	0.0/+5.0	+6.0	−3.0/−1.5	N/A

the electrically insulated main solid fuel. The main component of both filaments is PLA, expecting the smooth fuel regression without gaps between the sensor structure and the main solid fuel during burns. The slab fuels are manufactured using a Raise3D N1 Dual. This model is a multi-material FFF 3D printer with two separate extruders. In the additive manufacturing process, the slab fuels were layered from the top surface to the thickness direction. The layer thickness in the modeling was 0.15 mm for all designs.

Figure 6 depicts the two designs of the cylindrical fuel grains. In the additive manufacturing process, the cylindrical grains are layered from a base to their length direction. The layer thicknesses of Designs A and B were 0.05 mm and 0.10 mm, respectively. The outer side face was coated by an epoxy resin Z-1 by Nissin Resin Co., Ltd. in the post-process to ensure airtightness. Design A has three ladder-shaped resistor structures, but these resistors were not used in the experiments due to poor modeling accuracy. Moreover, their screw interface lost the conductivity due to the epoxy coating.

Solid fuels were ignited by the arc discharge between the two ignition wires, a small mass flow rate of GOX, and the gelatinous fuel placed on the fore-end of the inner surface of the fuel. The sheath wires that act as electrodes of the ignitor are fixed on the fuel using a non-woven fabric tape and an instant glue to securely fix the ignition wires over the ignition phase. The in-house arc discharge ignitor is triggered by the in-house LabVIEW sequence program.

2.6 Experimental conditions

Table 1 shows the important conditions and events in each time sequence of successful runs in firing. The expected burn time was 5.0 s for all runs. The burner or motor is ignited between −3.0 to −1.5 s under a small flow rate of GOX, and the open signal of the main valve is sent between 0 s and +5.0 s while that of the purge valve is sent from +6.0 s. The main and purge valve had a delay of 0.2–0.3 s and approximately 0.1 s, respectively. The high-speed camera was triggered at 0 s for the runs with the FX6000 (Camera 1) and -3 s for the other runs with the OS8-V3-S3 (Camera 2).

Table 2 Target regions of the optical fuel regression analysis.

Run #	S1	S2	S3	S4	S5
Start position [mm]	32.7	2.4	1.1	7.7	35.0
End position [mm]	93.6	91.8	27.8	26.9	98.0

3. Post-experimental analysis

3.1 Optical regression rate evaluation of rectangular slab fuel

As a post-experimental analysis of the acquired high-speed videos, the time-history of fuel regression is quantitatively evaluated using an in-house image recognition program coded by MATLAB R2019a. In the analysis program, the boundary of the binarized image frame is recognized as the fuel surface. The detailed process to acquire the time-history of the fuel regression is presented in the previous papers by the authors[13),14)]. In this investigation, the target fuel surface region of the analysis is expanded as possible to acquire the space-averaged fuel regression rate. Table 2 shows the axial regions used for the fuel surface detection in terms of the distance from the fore-end of the slab fuel. The region without contamination in the visualization window or strong emission at the fuel surface is selected for the fuel surface recognition. For runs #S2 to #S5, the high-speed video was not used for the fuel surface recognition until approximately +0.5 s. This is because the fuel surface could not be identified by the strong flame emission from the burning ignition wires and non-woven fabric tape used to fix them. As depicted in Figure 7, in actual surface detections, there exist many noise data points mainly due to the emission of a leaked flame between the window and the fuel side surface. However, the time trace of the minimum values of the

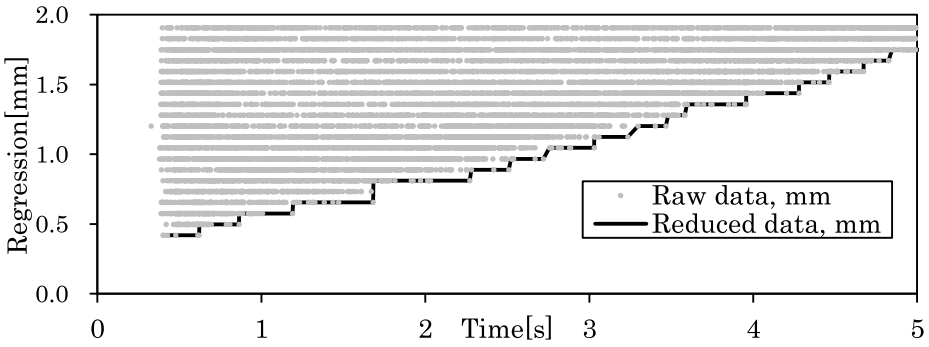

Figure 7 Typical noise reduction of time-history of fuel surface position.

Table 3 Summary of experimental results.

Run #	S1	S2	S3	S4	S5	C1	C2	C3
$t_e - t_s$ [s]	4.971	5.042	4.994	4.942	4.978	4.518	5.029	4.500
m_{oave} [g·s^{-1}]	17.0	35.3	36.8	34.4	52.1	14.7	23.3	59.3
$r_e - r_s$ [mm]	$0.08^{+0.42}_{0}$	$1.51^{+0.15}_{0}$	$1.72^{+0.19}_{0}$	$1.19^{+0.22}_{0}$	$1.75^{+0.29}_{0}$	2.06	3.02	4.47
$G_{s,t}$ [kg·m^{-2}·s^{-1}]	46.0	120	126	120	178	79.0	112	239
$r_{s,t}$ [mm·s^{-1}]	$0.02^{+0.10}_{0}$	$0.30^{+0.33}_{0}$	$0.34^{+0.38}_{0}$	$0.24^{+0.29}_{0}$	$0.35^{+0.41}_{0}$	0.46	0.60	0.99

regression is continuous and monotonically increasing, likely because misdetection occurs only beneath the real fuel top surface. Therefore, these local minimum values are regarded as the real fuel surface, whereas the other data are eliminated. The instantaneous fuel regression rate is calculated by counting the time it takes for the fuel surface to regress by a thickness equivalent to 1 pixel. The acquired time-history of the remaining fuel thickness data is used also for the time-trace of oxidizer mass flux by combining with the time-history of oxidizer mass flow rate.

3.2 Regression rate evaluation of cylindrical lab-scale motor

For the cylindrical grains, only the space-time averaged fuel regression rate is evaluated. The regression rate is evaluated from the burn time and the increase of the space-averaged inner diameter of the grain. For the first run using Design A, this parameter is estimated from the mass of the water used to fill the fuel port. For the other runs, the space-averaged inner diameter is estimated from the density of the fuel grain calculated from the dimension and the mass before the post-process and the mass loss after the burn. In this work, the start of a burn, t_s is defined as the time when oxidizer mass flow rate reaches 10 % of the maximum oxidizer mass flow rate, with the reference to the thrust-based definition of the burn time of solid rocket propulsion[14]. The end of a burn, t_e is defined as the time when the mass flow rate starts to decrease or PN starts to decrease due to the opening of PV1, whichever comes first. The space-time averaged regression rate, $r_{s,t}$ and oxidizer mass flux, $G_{s,t}$ are calculated using the averaged diameter method[15] as

$$\dot{r}_{s,t} = \frac{r_e - r_s}{t_e - t_s} \tag{1}$$

$$G_{s,t} = \frac{4\dot{m}_{o_{ave}}}{\pi (r_e + r_s)^2} \tag{2}$$

where r_s and r_e refer to the inner diameters before and after the burn, respectively, and m_{0ave} refers to the time-averaged oxidizer mass flow rate over the burn time. The equivalent definitions of burn time and the space-time averaged regression rate and oxidizer mass flux are applied to the runs of the slab fuels though it should be noted that the region of the space-averaging is limited to that used for the fuel surface recognition.

4. Results and discussion

The firing experiments were successfully performed according to the sequence program except for C3. For this run, the post-chamber and nozzle plates eroded probably due to the impingement of the high-pressure hot gas so that a manual emergency stop was activated at +4.7 s. However, the measured fuel regression is regarded as the resultant data because there was no irregular regression in the fuel grain and the emergency stop safely worked. The recovery of PG1 and the decrease of PN suggesting the stop of the GOX supply and the start of purging were measured at approximately +4.76 s and +24.82 s, respectively. Table 3 shows the results of the firing experiments. The time-averaged oxidizer mass flow rate and the corresponding oxidizer mass flux ranged from 17.0 to 52.1 g·s^{-1} and from 46.0 to 178 kg·m^{-2}·s^{-1}, respectively, for the slab burner. Those for the cylindrical grain ranged from 17.0 to 52.1 g·s^{-1} and from 46.0 to 178 kg·m^{-2}·s^{-1}, respectively. The time-averaged oxidizer mass flux ranged between 14.7 and 59.3 kg·m^{-2}·s^{-1}. For the slab burner, the total fuel regression on this table is the difference of the fuel thickness before and after the burn that was measured by a caliper. Due to the roughness of the fuel top surface, the

positive errors are also shown on the table, and the corresponding errors are also shown in the result of $r_{s,t}$. These errors are now shown in the results of the cylindrical grains because the averaged fuel regression was evaluated using the mass-loss method or the water volume method.

Figure 8 shows the time-histories of fuel regression for the slab fuels. The fuel regression was optically measured over the burn only for S1, owning to the routing of the ignition wires from the pressure vessel beneath the bottom plate. However, the optical fuel regression measurement did not provide enough accuracy because of the low camera resolution of 0.065 mm per pixel compared to the resultant fuel regression of 0.08 mm. For the other runs, the ignition wires and the non-woven fabric tape disturbed the visualization so that the fuel surface detention started approximately from +0.3 s after blowing off the ignition wires. For S2, the fuel surface position was negative for the initial 709.60 ms. This is because the non-woven fabric tape remaining on the surface was recognized as the fuel surface.

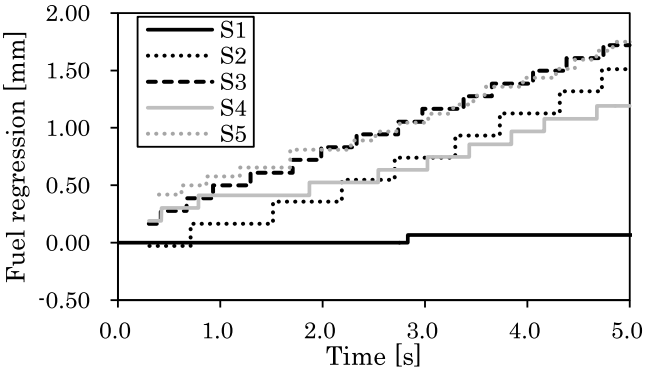

Figure 8 Time-histories of fuel surface position.

Figure 9 shows the instantaneous regression rate with the instantaneous oxidizer mass flux. These instantaneous parameters were calculated from the time-histories of fuel regression and oxidizer mass flow rate. The two series of space-time averaged regression rates, which are based on the high-seed videos and the measurement by caliper, respectively, are also plotted for comparison. The two space-time averaged regression rates agreed well with each other. The instantaneous regression rates had a large dispersion and did not seem to be correlated with instantaneous oxidizer mass flux during a run.

Figure 10 shows the space-time averaged fuel regression rates for cylindrical fuel grains C1–C3 with a conventional power fitting curve, compared to the behavior of the slab fuels. The space-time averaged fuel regression rate of the cylindrical grains follows the conventional power law[6]: $r_{s,t} = aG^n_{s,t}$, whereas the slab fuels did not follow this trend. For the cylindrical PLA grains, (a, n) was (0.022, 0.697). According to this fitting curve, the cylindrical grains have twice larger regression rates than the slab fuels despite the same PLA. According to the diffusion-limited theory by Marxman et al.[16], convective heat transfer which is the dominant heat transfer mechanism of fuel regression in the

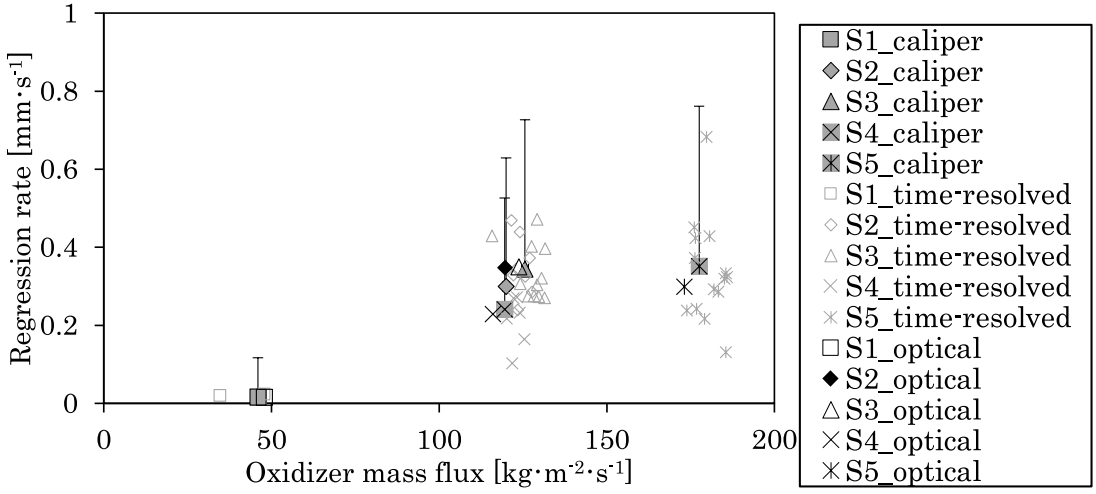

Figure 9 Fuel regression behavior for slab fuels.

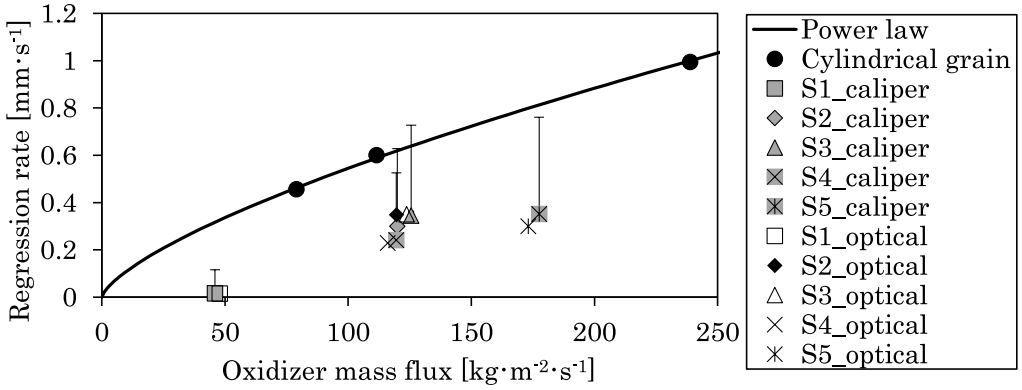

Figure 10 Comparison of fuel regression behavior between cylindrical grains and slab fuels.

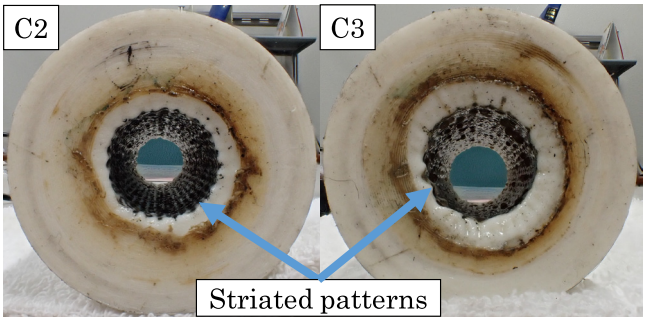

Figure 11 Striated patterns on the inner surface of cylindrical grains.

oxidizer-rich condition is connected to the skin friction coefficient through Reynolds analogy. A flat plate and a cylindrical pipe have different skin friction coefficients of $C_f/2 = 0.0225Re_\sigma^{-0.25}$ and $C_f/2 = 0.03325Re_\sigma^{-0.25}$ for turbulent boundary layer[17], respectively, but this difference can only explain a 45 % increase of fuel regression, even when considering the increase of fuel mass flux for cylindrical grains. As shown in Figure 11, for C2 and C3, the inner surface of the solid fuel grain had surface roughness with a striated pattern to the length (layer) direction, which was not observed on the slab fuels. The mechanism forming the roughness is not clarified so far, but this roughness should also contribute to the increase of fuel regression by that of the surface area.

An important key factor that can be correlated with the difference in the regression rates is the layer direction of the solid fuel to the oxidizer flow direction. In the modeling of FFF, the anisotropy of material properties within the same layer and between different layers is widely recognized especially in the mechanical and electrical properties. For general FFFs, the cross-section of a deposited line is an elliptical column, and there are elongate lines of voids along the line[18]. Therefore, the void-area ratio is different between the same layer and different layers so that tensile strength and electrical conductivity between different layers are lower than those within a layer. The adhesion strength between lines is also different between the same layer and different layers. In this experimental campaign, the layer direction of the slab fuels is normal to the oxidizer flow whereas that of the cylindrical grain is parallel to the oxidizer flow. In future work, the existence of the anisotropy of fuel regression behavior should be confirmed while considering the other potential causes included in the differences in the experimental conditions such as the shape of combustors.

5. Conclusions

This research investigated the fundamental fuel regression behavior of additively manufactured PLA fuels to be used for the main solid fuel in the demonstration of the advanced closed-loop control of hybrid rocket propulsion. Firing experiments were carried out with the slab burner and the small-scale cylindrical test motor. The solid fuels for these two combustors were manufactured by FFF and fired under the axial oxidizer injection. They were the rectangular slab fuels with the layer direction normal to the flow direction and the cylindrical fuel grains with the layer direction parallel to the flow direction, respectively. For the former condition, both the space-time averaged did not have the conventional oxidizer mass flux power law. The slab fuels continuously regressed increasing with burn time, but the instantaneous fuel regression rates dispersed when they are plotted against instantaneous mass flux. On the other hand, for the latter condition, the cylindrical fuel grains had at most twice larger regression rates than the slab fuels, and the space-time averaged fuel regression rate followed the conventional power law. For the two cases with large oxidizer mass flow rates, the inner surface after the burns had surface roughness with a striated pattern unique to cylindrical grains. The large difference in fuel regression can suggest the anisotropy of fuel regression manufactured by FFF due to the difference in the angle between the layer direction and the oxidizer flow direction. Possible factors causing the anisotropy of fuel regression are those of void structure between deposited lines, its area ratio, and adhesion strength, and it is expected to clarify the characteristics of the anisotropy in fuel regression and how that is caused by these possible factors in the future work.

Acknowledgment

This research was financially supported by Japan Society for the Promotion of Science Grants-in-Aid for Scientific Research grant number 18K13926, the Foundation for the Promotion of the Industrial Explosives Technology, the Hattori Hokokai Foundation, and Japan Keirin Autorace Foundation. The authors express appreciation to Assoc. Prof. Tomohide Yabuki at the Kyushu Institute of Technology for providing us with the opportunity to use the high-speed OS8-V3-S3 camera owned by his laboratory.

References

1) K. Ozawa and T. Shimada, J. Propuls. Power., 36, 400–414 (2020).
2) K. Ozawa and T. Shimada, J. Propuls. Power., 37, 86–99 (2021).
3) K. Ozawa and T. Shimada, J. Fluid Sci. Technol., 13, 1–18 (2018).
4) K. Ozawa and T. Shimada, J. Propuls. Power., 35, 94–108 (2019).
5) M. J. Chiaverini, N. Serin, D. L. Johnson, Y. Lu, K. K. Kuo, and G. A. Risha, J. Propuls. Power., 16, 25–132 (2000).
6) M. J. Chiaverini and K. K. Kuo, "Fundamentals of Hybrid Rocket Combustion and Propulsion", AIAA, Reston (2007).
7) M. F. Galfetti and L. G. Colombo, International Patent Classification, PCT/EP2014/065640 (2015).
8) F. S. Mechentel, B. R. Hord, and B. J. Cantwell, J. Propuls. Power., 36, 763–772 (2020).
9) S. D. Zilwa, G. Zilliac, M. Reinath, and A. Karabeyoglu, J. Propuls. Power., 20, 684–689 (2004).
10) K. Kitagawa and S. Yuasa, J. JSASS, 54, 242–249 (2006). (in Japanese).
11) H. Nagata, M. Ito, T. Maeda, M. Watanabe, T. Uematsu, T. Totani, and I. Kudo, Acta Astronaut., 59, 253–258 (2006).
12) Y. Saito, T. Yokoi, H. Yasukochi, K. Soeda, T. Totani, M. Wakita, and H. Nagata, J. Propuls. Power., 34, 247–259 (2017).

13) K. Ozawa, H. Wang, T. Yoshino, and N. Tsuboi, 70th Acta Astronaut., 187, 89−100 (2021).
14) G. P. Sutton and O. Biblarz, "Rocket Propulsion Elements", 7th ed., 417−473, John Wiley & Sons, New York (2001).
15) A. M. Karabeyoglu, B. J. Cantwell, and G. Zilliac, J. Propuls. Power., 23, 737−747 (2007).
16) G. A. Marxman, Proc. Combust. Inst., 10, 1337−1349 (1965).
17) H. Schlichting, "Boundary Layer Theory", 7th ed., 596−667, McGraw-Hill, New York (1979).
18) M. Hebda, C. MecIloy, B. Whiteside, F. Caton-Rose, and P. Coats, Addit. Manuf., 27, 99−108 (2019).